

Deep Learning Generates Synthetic Cancer Histology for Explainability and Education

James M. Dolezal¹, Rachele Wolk², Hanna M. Hieromnimon¹, Frederick M. Howard¹, Andrew Srisuwananukorn³, Dmitry Karpeyev⁴, Siddhi Ramesh¹, Sara Kochanny¹, Jung Woo Kwon², Meghana Agni², Richard C. Simon², Chandni Desai², Raghad Kherallah², Tung D. Nguyen², Jefree J. Schulte⁵, Kimberly Cole², Galina Khramtsova², Marina Chiara Garassino¹, Aliya N. Husain², Huihua Li², Robert Grossman⁶, Nicole A. Cipriani^{2*}, Alexander T. Pearson^{1*}

¹Section of Hematology/Oncology, Department of Medicine, University of Chicago Medicine, Chicago, IL

²Department of Pathology, University of Chicago Medicine, Chicago, IL

³Tisch Cancer Institute, Icahn School of Medicine at Mount Sinai, New York, NY

⁴DV Group, LLC, Chicago, IL, USA

⁵Department of Pathology and Laboratory Medicine, University of Wisconsin at Madison, Madison, WI, USA

⁶University of Chicago, Center for Translational Data Science, Chicago, IL

* Correspondence to nicole.cipriani@bsd.uchicago.edu and alexander.pearson@bsd.uchicago.edu

Abstract

Artificial intelligence (AI) methods including deep neural networks can provide rapid molecular classification of tumors from routine histology with accuracy that can match or exceed human pathologists. Discerning how neural networks make their predictions remains a significant challenge, but explainability tools can help provide insights into what models have learned when corresponding histologic features are poorly understood. Conditional generative adversarial networks (cGANs) are AI models that generate synthetic images and illustrate subtle differences between image classes. Here, we describe the use of a cGAN for explaining models trained to classify molecularly-subtyped tumors, exposing associated histologic features. We leverage cGANs to create class- and layer-blending visualizations to improve understanding of subtype morphology. Finally, we demonstrate the potential use of synthetic histology for augmenting pathology trainee education and show that clear, intuitive cGAN visualizations can reinforce and improve human understanding of histologic manifestations of tumor biology.

Main

Accurate diagnosis from histopathology is the first step in the evaluation of many cancers, with management pivoting upon a tumor's morphologic classification. Molecular profiling through analysis of DNA mutations, RNA fusions, and gene expression is also increasingly utilized, as a tumor's molecular subtype may inform prognosis or allow targeted therapies. Deep neural networks (DNN) can classify tumors from pathologic images with high accuracy, and several studies have shown that these models can also detect actionable genetic alterations and gene expression from tumor histology even when the associated histopathological phenotype is unknown¹. DNNs are however limited by their lack of predictive transparency, contributing to an explainability crisis as the scientific community attempts to interpret these models^{2,3}. When a neural network trained to detect molecular subtype performs well but the corresponding histologic features are poorly understood, explainability tools may provide insights into what the model learned and help ensure predictions are based on biologically plausible image features.

Conditional generative adversarial networks (cGANs) are AI models that can generate images prototypical of a given class and create smooth transitions between classes^{4,5}. As an explainability tool, they differ from other methods in that they offer a visually clear, easily interpretable look into class differences^{6,7}. Recent work has shown that generative networks can create realistic histologic images⁸⁻¹¹. Here, we show that cGAN visualizations can provide nuanced insights into the histologic correlates for a given molecular state and improve understanding of subtype morphology. Furthermore, we show that these synthetic histologic visualizations are intuitive enough to improve pathology trainee classification of a rare tumor subtype.

Our approach starts with training DNN classification and cGAN models on digital pathology images (**Fig. 1A**). cGANs generate an image from the combination of a seed – a vector of random numbers that determines what the image will broadly look like – and a class label, which influences the image toward one class or another (**Fig. 1B**). The class label is converted into an embedding, a vector of numbers learned through training that encodes the essence of the class, and passed to each layer of the cGAN. For a given seed, synthetic histologic images and corresponding classifier predictions are generated for each class. If the predictions are strong and match the cGAN class label, the seed has strong classifier concordance, and if the predictions are weak but match the cGAN class label, the seed has weak concordance (**Fig. 1C**). Side-by-side, classifier-concordant image pairs illustrate histologic differences responsible for changes in classifier prediction, assisting with model explainability. To create an image in transition from one class to another, we perform a linear interpolation between two class embeddings and use the interpolated embedding for cGAN conditioning; using the same seed but gradually interpolating the embedding creates class-blended images that gradually shift from one class to another (**Fig. 1D**).

We trained a classifier and cGAN for non-small cell lung cancer (NSCLC) conditioned on adenocarcinoma vs. squamous cell carcinoma, as this is a well-described histologic phenotype suitable for assessing feasibility of the approach when the expected morphologic differences are known (**Fig. 1E** and **Supplementary Fig. 1**). Expert pathologist assessment revealed that images were realistic and consistent with the cGAN class labels (**Supplementary Fig. 2**). We repeated the approach for breast cancer estrogen receptor (ER) status, chosen because ER status influences morphologic phenotype on standard hematoxylin and eosin (H&E) stained slides^{12,13}, but the morphologic correlates are incompletely characterized (**Fig. 1F**). Two expert breast pathologists concluded that the synthetic ER-negative images had higher grade, more tumor-infiltrating lymphocytes, necrosis, and/or apocrine differentiation compared with ER-positive images (**Supplementary Fig. 3**).

Finally, we trained a cGAN on thyroid neoplasms, conditioned on whether the tumor had $BRAF^{V600E}$ -like or RAS -like gene expression (**Fig. 1G**). $BRAF$ - RAS gene expression score, a score between -1 ($BRAF^{V600E}$ -like) and +1 (RAS -like), correlates with thyroid neoplasm histologic phenotype and can be used to distinguish malignant papillary thyroid carcinomas (PTC) from the low-risk non-invasive follicular thyroid neoplasms with papillary-like nuclear features (NIFTP), despite the fact that these entities are challenging to distinguish even by experienced pathologists¹⁴⁻¹⁷. cGAN visualizations illustrate subtle morphologic changes associated with $BRAF$ - RAS spectrum, including nuclear changes (enlargement, chromatin clearing, membrane irregularities), architectural changes (elongated follicles, papillae), colloid changes (darkening, scalloping), and stromal changes (fibrosis, calcification, ossification) (**Supplementary Fig. 4**). Class blending provides realistic histologic images that gradually transition from $BRAF^{V600E}$ -like morphology to RAS -like morphology (**Fig. 1H**), and predictions of these blended images smoothly change from $BRAF^{V600E}$ -like to RAS -like (**Fig. 1I**).

Layer blending can provide deeper insights into class-specific morphology, as passing different embeddings to each layer in the cGAN offers a method for controlling the scale at which an image is influenced to be more like one class or another (**Fig. 2A**). For example, in **Fig. 2B**, a synthetic RAS -like image is shown as image B1, and a $BRAF^{V600E}$ -like image from the same seed is shown as image B6. Passing the $BRAF^{V600E}$ -like embedding only to layers 4-6, as shown in image B2, results in a decrease in size and variation in morphology of the follicles compared to image B1, but the prediction does not move in a $BRAF^{V600E}$ -like direction. Passing a $BRAF^{V600E}$ -like embedding to layers 7-9, as shown in Image B3, instead results in a minimal increase in chromatin clearing and a more eosinophilic color profile, and the classifier prediction has now moved closer to the $BRAF^{V600E}$ -like end of the spectrum. In image B4, setting layers 10-12 to $BRAF^{V600E}$ -like results in subtle changes to the stroma, resulting in a more ropey appearance to the collagen as well as a more eosinophilic color profile.

We tested the use of synthetic histology to augment pathology trainee education by creating a cGAN-based educational curriculum illustrating the $BRAF$ - RAS spectrum in thyroid neoplasms (**Fig. 2C**). Six pathology residents first received a standard educational lecture on thyroid neoplasms, including discussion of NIFTP subtype and differences in $BRAF^{V600E}$ -like and RAS -like morphology. Residents completed a 96-question pre-test comprised of images of real tumors from a University of Chicago dataset, predicting whether images were $BRAF^{V600E}$ -like (PTC) or RAS -like (NIFTP). Residents then participated in a one-hour cGAN-based educational session, which included image pairs of synthetic $BRAF^{V600E}$ -like and RAS -like images generated from the same seed (**Fig. 2D**), video interpolations showing the gradual transition from $BRAF^{V600E}$ -like to RAS -like (**Supplementary Data**), and a computer-based interface in which residents could interactively generate synthetic images. Following the teaching session, residents completed a 96-question post-test comprised of real images from different cases than the pre-test. After the one-hour educational session, resident accuracy on real pathologic images significantly improved from 72.7% to 79.0% ($p = 0.011$) (**Fig. 2E**).

In summary, cGANs can generate realistic, class-specific histologic images, and exploring visualizations from images with high classifier concordance provides an intuitive tool for deep learning model explainability. Class blending via embedding interpolation yields realistic images with smooth transitions between classes, and layer blending reveals unique morphological constructs at architectural, cellular, and stromal levels. Synthetic histology not only offers an approach to model explainability, but can also provide new, hypothesis-generating insights into histologic associations with molecularly-defined tumor subtypes. Finally, synthetic histology can also be an effective teaching aid, capable of improving trainee recognition of histologic classes in a rare cancer subtype.

Methods

Dataset description

The Lung cGAN was trained on 941 whole-slide images (WSI) from The Cancer Genome Atlas (TCGA), including 467 slides from the lung adenocarcinoma project (TCGA-LUAD) and 474 slides from the lung squamous cell carcinoma project (TCGA-LUSC) (<https://portal.gdc.cancer.gov/>). Validation was performed on 1,306 WSIs from the Clinical Proteomic Tumor Analysis Consortium (CPTAC) lung adenocarcinoma (CPTAC-LUAD) and lung squamous cell carcinoma (CPTAC-LSCC) collections (<https://www.cancerimagingarchive.net/collections/>). The Breast cGAN was trained on 1,048 WSIs from The Cancer Genome Atlas (TCGA-BRCA), including 228 estrogen receptor (ER) negative tumors and 820 ER-positive tumors. Validation was performed on 98 WSIs from CPTAC, including 26 ER-negative and 72 ER-positive tumors. The Thyroid cGAN was trained on 369 WSIs from The Cancer Genome Atlas (TCGA-THCA), including 116 *BRAF*^{V600E}-like tumors (where *BRAF-RAS* gene expression score is less than 0) and 271 *RAS*-like tumors (where *BRAF-RAS* gene expression score is greater than 0). Validation was performed on an institutional dataset of 134 tumors, including 76 *BRAF*^{V600E}-like PTCs and 58 *RAS*-like NIFTPs.

Image processing

For the classifier models, image tiles were extracted from WSIs with an image tile width of 302 μm and 299 pixels using Slideflow¹⁸. For the breast and lung cGANs, image tiles were extracted with an image tile width of 400 μm and 512 pixels. For the thyroid cGAN, image tiles were extracted at 302 μm and 512 pixels. Background was removed via grayscale filtering, Otsu's thresholding, and gaussian blur filtering. Gaussian blur filtering was performed with a sigma of 3 and threshold of 0.02. Image tiles were extracted from within pathologist-annotated regions of interest (ROIs) to maximize cancer-specific training.

Classifier training

We trained deep learning classification models based on an Xception architecture, using ImageNet pretrained weights and two hidden layers of width 1024, with dropout ($p = 0.1$) after each hidden layer. Models were trained with Slideflow using the Tensorflow backend with a single set of hyperparameters and category-level mini-batch balancing (**Supplementary Table 1**). Training images were augmented with random flipping and cardinal rotation, JPEG compression (50% chance of compression with quality level between 50-100%), and gaussian blur (10% chance of blur with sigma between 0.5-2.0). Binary categorization models (lung and breast classifiers) were trained with cross-entropy loss, and the thyroid BRS classifier was trained with mean squared error loss. Models are first trained with site-preserved cross-validation¹⁹, then a final model is trained across the full dataset and validated on an external dataset.

cGAN training

Our cGAN architecture is an implementation of StyleGAN2, minimally modified to interface with the histopathology deep learning package Slideflow and allow for easier embedding space interpolation⁴. The lung cGAN was conditioned on the binary category of adenocarcinoma vs. squamous cell carcinoma, and the breast cGAN was conditioned on the binary category of ER-negative vs. ER-positive. The thyroid cGAN was conditioned on a binary categorization of the continuous *BRAF-RAS* score, discretized at 0 into *BRAF*^{V600E}-like (less than 0) or *RAS*-like (greater than 0).

The lung cGAN was trained on 4 A100 GPUs for 25,000 kimg (25 million total images) starting with random weight initialization. The breast cGAN was trained on 4 A100 GPUs for 10,000 kimg (10 million total images), and the thyroid cGAN was trained on 2 A100 GPUs for 12,720 kimg (12.7 million total images), stopped at this time point due to model divergence with further training. All cGANs were trained with an R1 gamma of 1.6384, batch size of 32, and using all available augmentations.

Classifier concordance

To assess classifier concordance for a cGAN and an associated classifier, the cGAN generates an image for each class using the same seed. The generated images are center-cropped and resized to match the same histologic magnification as the associated classifier, and the classifier creates predictions for each image. Predictions are considered “strong” if the post-softmax value is greater than 0.75 for the predicted class, and “weak” if the post-softmax value for the predicted class is less than 0.75. For the thyroid BRS classifier which uses a continuous outcome, predictions are considered “strong” if the raw prediction is less than -0.5 or greater than 0.5, and “weak” if the prediction is between -0.5 and 0.5. A given seed is defined as strongly concordant if the classifier predictions match the cGAN class labels for both images and the predictions are both strong. A seed is weakly concordant if the classifier predictions match the cGAN class labels, but either prediction is weak. A seed is non-concordant if the classifier predictions do not match the cGAN class labels.

cGAN class and layer blending

To create class-conditional images, cGAN class labels are projected into an embedding space before conditioning the network, with the projection learned during training. After training, each class label has a single associated embedding vector. To create class-blended images, we perform a linear interpolation between class embeddings and use these interpolated embeddings for network conditioning while holding the cGAN seed constant. We create layer-blended images by passing different class embeddings to each cGAN network layer while holding the cGAN seed constant.

Pathologist assessment of cGAN images

Domain-expert pathologists reviewed at least 50 strongly-concordant synthetic histologic images to assess realism, variety, and consistency with cGAN class labels. Pathologists first reviewed the images in a blinded fashion without knowledge of the associated cGAN labels. Lossless, PNG images were viewed at the full 512 x 512 px resolution. Pathologists then reviewed the strongly-concordance synthetic image pairs side-by-side with knowledge of the cGAN labels to assess consistency of the synthetic images with biological expectations for the associated class labels. Pathologists described histologic differences between each image pairs and provided an overall summary of thematic differences between classes.

cGAN educational session

Six pathology residents were recruited for this study via email. No sample-size calculation was performed prior to recruitment. Participating residents received a one-hour lecture as a part of their core educational curriculum discussing the histopathological diagnosis of thyroid neoplasms, including a discussion of differentiating between malignant papillary thyroid carcinomas (PTCs), including follicular-variant PTCs, and benign non-invasive follicular thyroid neoplasms with papillary-like nuclear features (NIFTP). A discussion of the molecular association between PTCs and *BRAF*^{V600E} mutations, and NIFTPs and *RAS* mutations, was also included.

Pathology residents then took a pre-test based on real images from 96 cases at the University of Chicago, including 48 PTCs (both classic and follicular-variant) and 48 NIFTPs. The trained BRS classifier model

generated predictions across all whole-slide images, and for each case, three strongly-predicted image tiles (prediction less than -0.5 or greater than 0.5) were randomly selected and merged side-by-side, and three weakly-predicted image tiles (prediction between -0.5 and 0.5) were randomly selected and merged, resulting in two merged image trios for each of the 96 cases. The pre-test was comprised of weak and strong image trios for 24 PTCs and NIFTPs, and residents were asked to predict whether the image trios came from a *BRAF*^{V600E}-like tumor (PTC) or *RAS*-like tumor (NIFTP).

Residents then participated in a one-hour cGAN-based educational curriculum. The curriculum was developed by first calculating classifier concordance for 1000 seeds and identifying the strongly-concordant seeds. *BRAF*^{V600E}-like and *RAS*-like image pairs for the 412 strongly-concordant seeds were reviewed by a domain expert pathologist, and 46 were chosen for inclusion in the teaching session. Video interpolations were generated and shown for seven of these seeds. The educational session was structured as a PowerPoint presentation, using only synthetic histologic image pairs and video interpolations to highlight important morphologic differences associated with the BRS spectrum. Residents also had access to a computer workstation loaded with an interactive visualization of cGAN generated images and class blending, to supplement the visualizations shown in slideshow format.

Finally, residents completed a post-test comprised of 96 images from 48 different cases than the pre-test, and resident classification accuracy was compared using a one-sided paired T-test.

Data availability

All data and associated accession numbers used for training is included in this repository, and can be additionally accessed directly at <https://portal.gdc.cancer.gov/> and <https://www.cancerimagingarchive.net/collections/> using the accession numbers provided in the **Supplementary Data**. Restrictions apply to the availability of the internal University of Chicago thyroid dataset, but all requests will be promptly evaluated based on institutional and departmental policies to determine whether the data requested are subject to intellectual property or patient privacy obligations. The University of Chicago dataset can only be shared for non-commercial academic purposes and will require a data user agreement.

Code availability

All code and models are made publicly available with an interactive user interface for class blending and latent space navigation at <https://github.com/jamesdolezal/histologic-sheep>. The user interface provided is the same interface used during the educational teaching session.

Ethics statement

Educational study was reviewed by institutional IRB and deemed minimal risk, exempt from protocol approval and requirement for informed consent.

Figure Legends

Figure 1. cGANs illustrate molecular states expressed in tumor histopathology with synthetic histology. (a) For a given set of training data, two models are trained – a conditional generative adversarial network (cGAN), which generates images, and a classification model, which predicts histologic class from an image. (b) cGANs create synthetic images from a seed of random noise and a class label, passed to each layer in the network through an embedding. Synthetic images are then classified by the trained classifier. (c) For a given seed, synthetic images are generated for each histologic class, and the classifier creates predictions for each image. Seeds for which predictions match the GAN labels are classifier-concordant. Visualizing classifier-concordant image pairs side-by-side allows one to appreciate the histologic features responsible for classifier predictions, providing a tool for model explainability and education. (d) Class-blended images are generated by interpolating between class embeddings while holding the seed constant. (e) A cGAN was trained on lung adenocarcinoma vs. squamous cell carcinoma. Classifier concordance for 1000 seeds was 31.1% strong, 27.0% weak, and 41.9% non-concordant. (f) A second cGAN was trained on breast cancer estrogen receptor (ER) status determined by immunohistochemistry (IHC). Classifier concordance for 1000 seeds was 25.9% strong, 10.0% weak, and 64.1% non-concordant. (g) A final cGAN was trained on thyroid neoplasm *BRAF-RAS* gene expression score (BRS). Classifier concordance for 1000 seeds was 41.2% strong, 36.2% weak, and 22.6% non-concordant. (h) Illustration of class blending performed for a strongly-concordant Thyroid cGAN seed, transitioning from *BRAF*^{V600E}-like to *RAS*-like. (i) Example class-blended images for the Lung and Breast cGANs. (j) Predictions smoothly transition during class blending.

Figure 2. Class and layer blending reveals distinct features of *BRAF*^{V600E}-like and *RAS*-like thyroid neoplasms and augments trainee education. (a) cGANs can create synthetic layer-blended images by conditioning the network using different embeddings at each layer. (b) Layer blending with a seed from the Thyroid cGAN reveals different morphologic changes associated with the *RAS*-like and *BRAF*^{V600E}-like gene expression spectrum. Each image includes a corresponding classifier prediction, from -1 (*BRAF*^{V600E}-like) to +1 (*RAS*-like). Image B1 is a fully *RAS*-like image, and Image B6 is a fully *BRAF*^{V600E}-like image. Images B2-B5 are generated by using different class embeddings at each cGAN layer. Examining the resulting morphologic changes that occur when passing the *BRAF*^{V600E}-like embedding to different layers illustrates different types of morphologic changes associated with the *BRAF*^{V600E}-*RAS* spectrum. (c) Schematic for creating GAN-based educational curriculum. (d) Schematic for assessing effect of cGAN-based educational session on ability for pathology trainees to accurately classify images from real thyroid neoplasms. (e) Example cGAN image pairs included in the educational curriculum which exemplify the histologic features associated with the *BRAF-RAS* gene expression spectrum, illustrating changes in the quality of the stroma (935, 107), nuclear enlargement and chromatin clearing (all seeds), scalloping of colloid (130, 107) and well-formed papillae (197). (f) Trainee classification accuracy on real images significantly improved after the teaching session, from 72.7% to 79.0% ($p = 0.011$).

References

1. Fu, Y. *et al. Nat. Cancer* **1**, 800–810 (2020).
2. Ghassemi, M., Oakden-Rayner, L. & Beam, A. L. *Lancet Digit. Health* **3**, e745–e750 (2021).
3. Reddy, S. *Lancet Digit. Health* **4**, e214–e215 (2022).
4. Karras, T. *et al. in Proc. CVPR* (2020).

5. T. Karras, S. Laine, & T. Aila. in *2019 IEEE/CVF Conference on Computer Vision and Pattern Recognition (CVPR)* 4396–4405 (2019). doi:10.1109/CVPR.2019.00453.
6. Lang, O. *et al.* (2021) doi:10.48550/ARXIV.2104.13369.
7. Shih, S.-M., Tien, P.-J. & Karnin, Z. S. in *ICML* (2021).
8. Levine, A. B. *et al. J. Pathol.* **252**, 178–188 (2020).
9. McAlpine, E., Michelow, P., Liebenberg, E. & Celik, T. *J. Am. Soc. Cytopathol.* **11**, 123–132 (2022).
10. Zhao, J., Hou, X., Pan, M. & Zhang, H. *Comput. Biol. Med.* **149**, 105948 (2022).
11. Krause, J. *et al. J. Pathol.* **254**, 70–79 (2021).
12. Naik, N. *et al. Nat. Commun.* **11**, 5727 (2020).
13. Couture, H. D. *et al. NPJ Breast Cancer* **4**, 30 (2018).
14. Dolezal, J. M. *et al. Mod. Pathol.* **34**, 862–874 (2021).
15. Elsheikh, T. M. *et al. Am. J. Clin. Pathol.* **130**, 736–744 (2008).
16. Hirokawa, M. *et al. Am. J. Surg. Pathol.* **26**, 1508–1514 (2002).
17. Lloyd, R. V. *et al. Am. J. Surg. Pathol.* **28**, 1336–1340 (2004).
18. Dolezal, J., Kochanny, S. & Howard, F. (2022) doi:10.5281/zenodo.7301864.
19. Howard, F. M. *et al. Nat. Commun.* **12**, 4423 (2021).

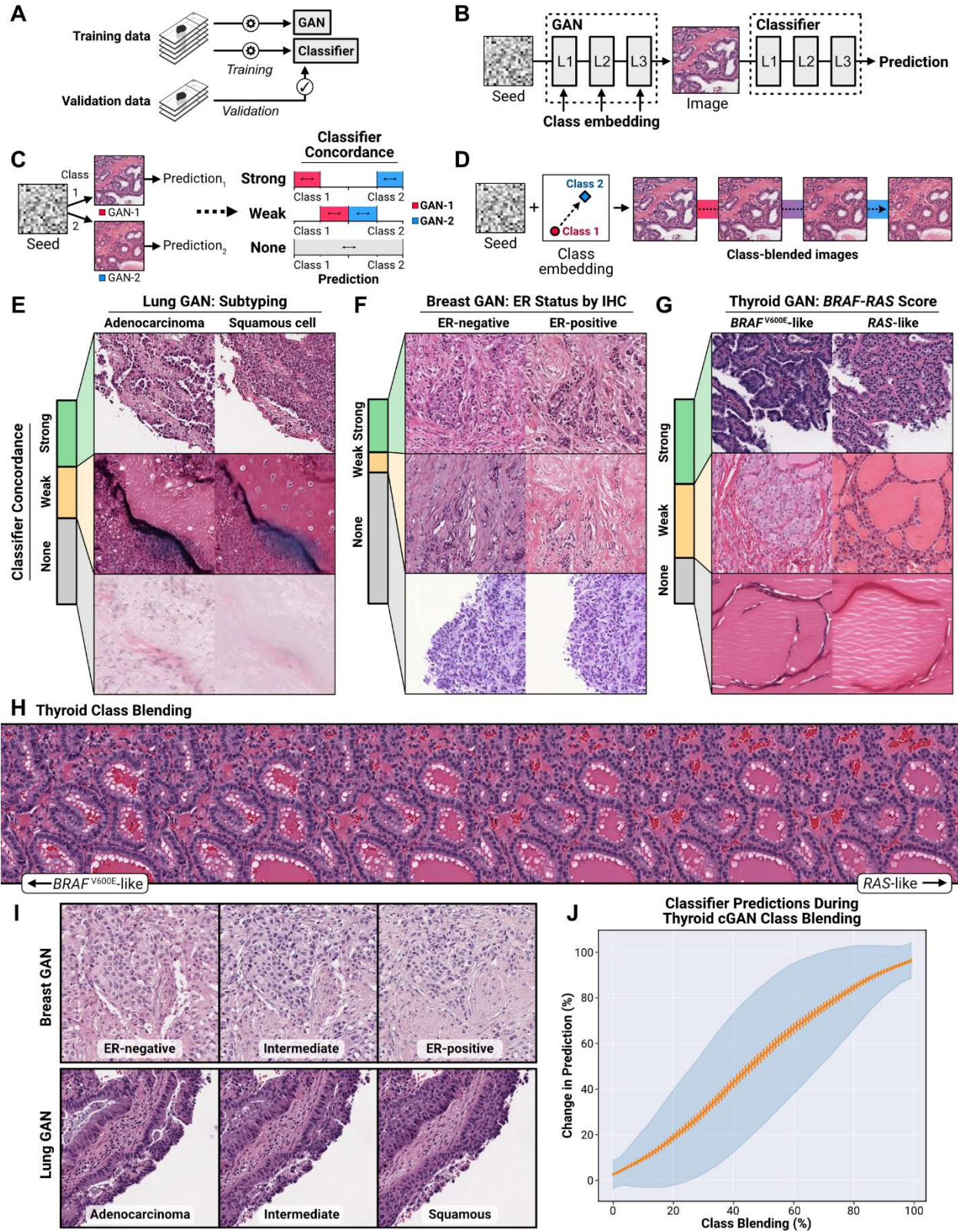


Figure 1

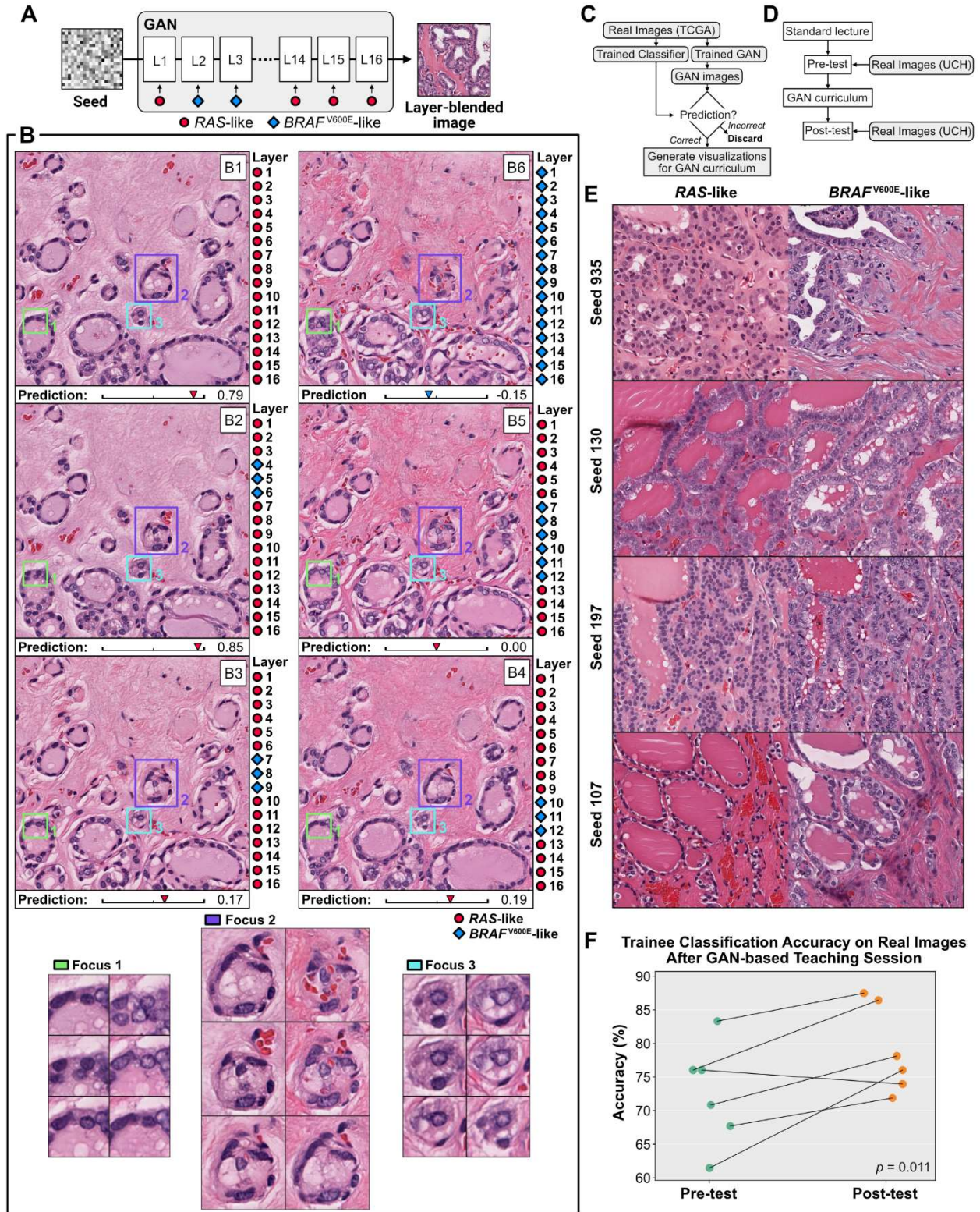


Figure 2